Comput Mech (2017) 60:393–408
DOI 10.1007/s00466-017-1398-z

ORIGINAL PAPER

A combined analytical formulation and genetic algorithm to analyze the nonlinear damage responses of continuous fiber toughened composites

Haemin Jeon[1] · Jaesang Yu[2] · Hunsu Lee[2] · G. M. Kim[3] · Jae Woo Kim[2] · Yong Chae Jung[2] · Cheol-Min Yang[2] · B. J. Yang[2]

Received: 1 November 2016 / Accepted: 5 March 2017 / Published online: 25 April 2017

Abstract Continuous fiber-reinforced composites are important materials that have the highest commercialized potential in the upcoming future among existing advanced materials. Despite their wide use and value, their theoretical mechanisms have not been fully established due to the complexity of the compositions and their unrevealed failure mechanisms. This study proposes an effective three-dimensional damage modeling of a fibrous composite by combining analytical micromechanics and evolutionary computation. The interface characteristics, debonding damage, and micro-cracks are considered to be the most influential factors on the toughness and failure behaviors of composites, and a constitutive equation considering these factors was explicitly derived in accordance with the micromechanics-based ensemble volume averaged method. The optimal set of various model parameters in the analytical model were found using modified evolutionary computation that considers human-induced error. The effectiveness of the proposed formulation was validated by comparing a series of numerical simulations with experimental data from available studies.

Keywords Fiber-reinforced polymer composites · Micromechanics · Genetic algorithm · Damage modeling · Failure mechanism

✉ Yong Chae Jung
ycjung@kist.re.kr

✉ Cheol-Min Yang
cmyang1119@kist.re.kr

✉ B. J. Yang
bj.yang@kist.re.kr

[1] Department of Civil and Environmental Engineering, Hanbat National University, 125 Dongseodae-ro, Yuseong-gu, Daejeon 34158, Republic of Korea

[2] Multifunctional Structural Composite Research Center, Institute of Advanced Composite Materials, Korea Institute of Science and Technology (KIST), 92 Chudong-ro, Bongdong-eup, Wanju-gun, Jeonbuk 55324, Republic of Korea

[3] Department of Civil and Environmental Engineering, Korea Advanced Institute of Science and Technology (KAIST), Daehak-ro 291, Yuseong-gu, Daejeon 34141, Republic of Korea

1 Introduction

It has been a number of years since composites (e.g., laminate, prepreg, towpreg etc.) have been introduced and developed in the fields of science and engineering, but they nevertheless remain costly [1]. Although diverse research on composites has been carried out in light of their large commercialized potential, the discovery of nano-materials has influenced the trend in research toward nano-composites, and away from conventional composites [2]. However, continuous fiber-reinforced composites are being used in more than 50% of aircraft frames, for example [3], and so it is evident that they are still important materials with strong potential for ongoing use in the future. Despite this, a theoretical understanding has not been fully established, due to the complexity of the compositions and elusive failure mechanisms [4].

In this study, we propose an effective three-dimensional (3D) material-damage model for fibrous composites, which combines analytical micromechanics and evolutionary computation that has recently been made possible by the development of computational intelligence. After studying the past three decades of theoretical and experimental studies on fibrous composites, we concluded that the paramount factors that contribute the toughness and failure behaviors in composites are the interface characteristics, debonding between

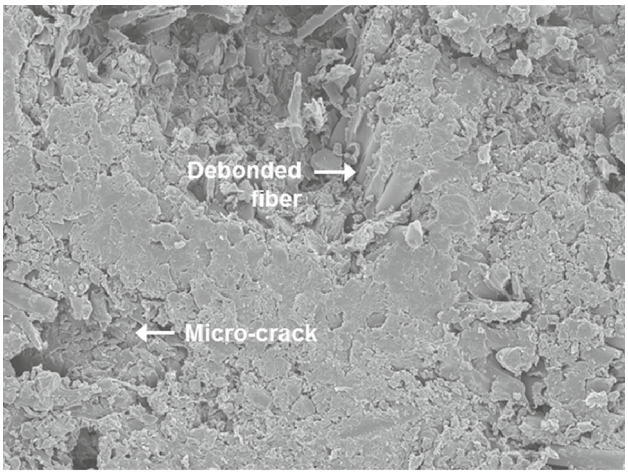

(a)

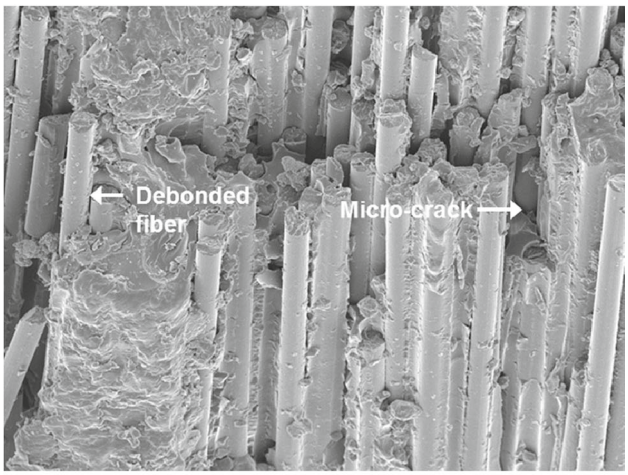

(b)

Fig. 1 SEM images of the typical fracture morphologies of fiber-reinforced polymer composites

the matrix and continuous fiber, and micro-cracks (see Fig. 1) [5].

The manifestation of each mechanism was modeled using the following well established methods: the ensemble-volume average (EVA) method [6,7], the weakened interface approach [8–10], the Weibull probability debonding method [11,12], and the continuum damage model for the nucleation of micro voids [13–15]. The micromechanics-based EVA method was first proposed by Ju et al. [6] to predict the effective elastic behaviors of multi-phase composites. A governing micromechanical ensemble-volume averaged field equation was developed, in which a heterogeneous composite is statistically assumed to be a homogenous solid independent of the shape of the representative volume element (RVE) [6]. In the micromechanical framework, the inter-inclusion interactions are ignored for mathematical simplicity. Ju et al. [7] extended the work to predict the mechanical behaviors of composites containing randomly located yet unidirectionally aligned circular fibers. Again, to allow a simple approximate analytical solution, the fibers were assumed to be infinitely long and equal-sized inclusion [7].

The Eshelby's tensor for an inclusion with a weakened interface was physically derived by Qu [8]. The weakened interface between the inclusions and the matrix was modeled by a spring layer of vanishing thickness, and the interfacial compliance in the tangential and normal directions was position independent [8]. Pyo and Lee [9] and Kim and Lee [10] explicitly modified the Eshelby's tensor for an infinite fiber-shaped inclusion considering interface effects. Probability approaches to modeling the debonding and microcrack phenomena were constructed by Lee [11], Lee and Simunovic [12], and Karihaloo [15]. By combining the micromechanical framework and probabilistic functions, various multi-level damage models have been developed to describe the different damage mechanisms [14,16,17]. It should be noted that the model parameters of the above-mentioned methods were estimated based on experimentally obtained stress–strain or load–displacement curves.

Each nonlinear model parameter set should be applied differently depending on the corresponding material combination. Nonetheless, the values of this fitting were found heuristically, and this kindled a controversy regarding the reliability and rigorousness of parameters. Above all, calculating interactions or correlations between experiments and simulations is typically the most time-consuming aspect.

Therefore, we proposed finding optimal sets of each parameter with an analytical formulation by applying evolutionary computation of the genetic algorithm (GA). Herein, additional components of human-induced error are included in the GA considering complexity and production characteristics of the composites. Each model parameter and range was determined by referring to past research and a numerical simulation performed independently in this study. To validate the approach proposed in the present study, experimental results for various circumstances were compared to the predicted values. It is believed that the present study helps to enhance understanding of damage phenomena in heterogeneous composites that contain continuous fiber. In addition, the developed analytical modeling and GA proposed in the study for fibrous composites have adaptive characteristics and are expected to exhibit high correlation with other material models.

2 A constitutive model for fibrous composites

2.1 3D material damage modeling with interface and fiber orientation

Let us start by considering a representative volume element (RVE) of composites composed of an isotropically elastic matrix (phase 0) and a transversely elastic continuous fiber,

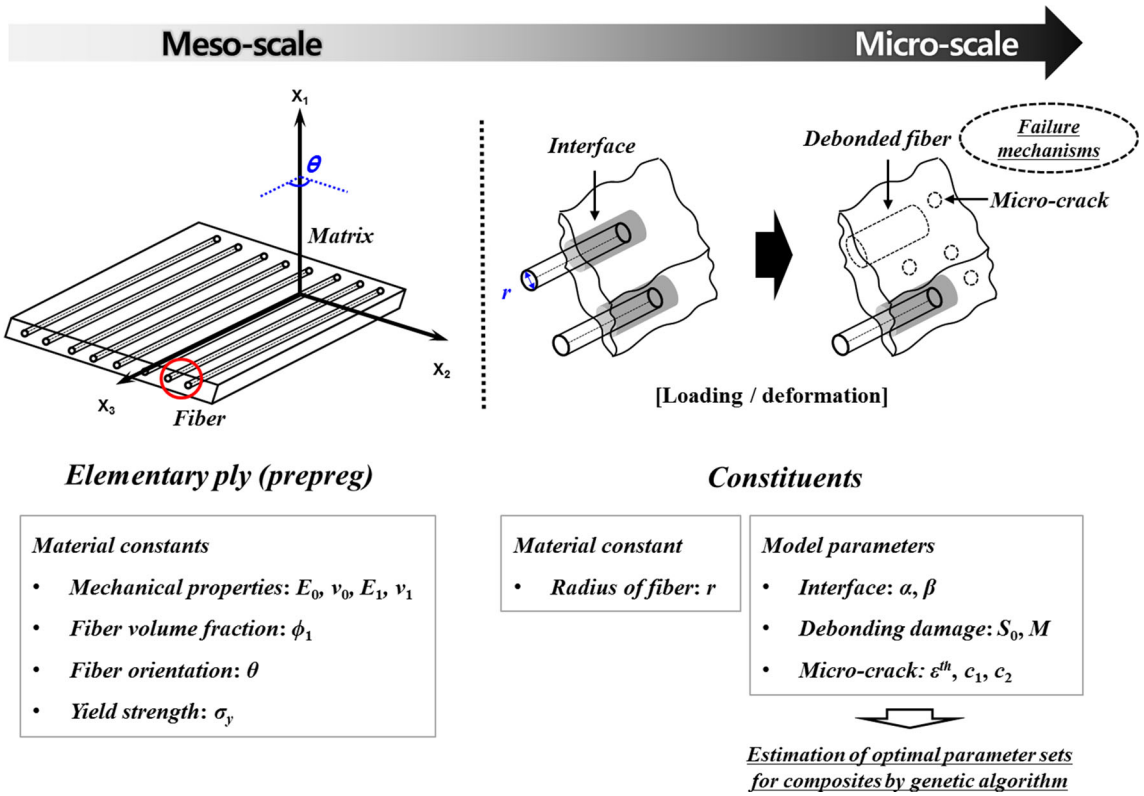

Fig. 2 A schematic illustration of the proposed material modeling of fibrous composites

with interface properties (phase 1). We note that the unidirectional (UD) fiber within the matrix is aligned in a 3-axis and is uniformly distributed, as exhibited in Fig. 2 [18]. It is assumed that the composite materials may experience failure due to damage under loading and increasing deformation [10]. As loading and deformation continue to increase, some UD fibers will incrementally lose their load-carrying capacity, and become debonded fibers (phase 2). In the literature [10,13,19], these debonded fibers (phase 2) are regarded as equivalent cylindrical voids [13], and this is adopted here as well. In addition, the micro-cracks (phase 3) produced by external loading/deformation are included in the present derivation by modeling them as randomly dispersed spherical voids.

The equivalence equation of the proposed multi-phase composites (matrix, fiber with interface properties, debonded fiber, and micro-crack) can be expressed as

$$\overline{\boldsymbol{\sigma}} = \mathbf{C}^* : \overline{\boldsymbol{\varepsilon}} \tag{1}$$

where $\overline{\boldsymbol{\sigma}}$ and $\overline{\boldsymbol{\varepsilon}}$ signify the averaged stress and strain. $\mathbf{C}^*$ is the effective stiffness tensor for continuous fiber-reinforced polymeric (FRP) composites, which can be derived based on the EVA method [6,12,17]:

$$\mathbf{C}^* = \mathbf{C_0} \cdot \left[\mathbf{I} + \sum_{q=0}^{3} \left\{ \phi_q \left(\mathbf{A}_q + \mathbf{S}_q \right)^{-1} \cdot \left[\mathbf{I} - \phi_q \mathbf{S}_q \cdot \left(\mathbf{A}_q + \mathbf{S}_q \right)^{-1} \right] \right\}^{-1} \right] \tag{2}$$

with

$$\mathbf{A}_q = \left(\mathbf{C}_1 - \mathbf{C_0} \right)^{-1} \cdot \mathbf{C_0} \tag{3}$$

where $\mathbf{C}_q$ and ϕ_q are the elasticity tensor and volume fraction of q-phase ($q = 0, \ldots, 3$); $\mathbf{I}$ denotes the four-rank identity tensor; $\mathbf{S}_q$ means the Eshelby's tensor for q-phase.

The interface layer property between the matrix and continuous fiber is modeled by the linear spring layer approach with a continuous traction yet a displacement jump [8,20]:

$$\eta_{ij} = \alpha \delta_{ij} + (\beta - \alpha)\, n_i n_j \tag{4}$$

where δ_{ij} and n_i represent the Kronecker delta and outward normal; α and β are the interface parameters, denoting the tangential and normal components of the compliance,

respectively [8]. With the help of the linear spring model, the modified Eshelby's tensor for a circular cylindrical fiber with interface properties (phase 1) can be written as [8,16]

$$\mathbf{S}_1 = \frac{1}{256r\,(1-v_0)^2}\left[S_{IK}^{(1)}\delta_{ij}\delta_{kl} + S_{IJ}^{(2)}\left(\delta_{ik}\delta_{jl}+\delta_{il}\delta_{jk}\right)\right] \tag{5}$$

with

$$\begin{aligned}
S_{11}^{(1)} &= 32r\left(-1+5v_0-4v_0^2\right) - 3\pi\mu_0\alpha \\
&\quad + 24\pi\,(1-2v_0)^2\,\lambda_0\beta + 3\pi\left(7-32v_0+32v_0^2\right)\mu_0\beta \\
S_{22}^{(1)} &= S_{12}^{(1)} = S_{21}^{(1)} = S_{11}^{(1)} \\
S_{13}^{(1)} &= 128v_0\,(1-v_0) + 48\pi\,(1-2v_0)\,\beta\,\{(1-2v_0)\,\lambda_0 \\
&\quad - v_0\mu_0\}\,,\ S_{23}^{(1)} = S_{13}^{(1)}\,, \\
S_{31}^{(1)} &= S_{32}^{(1)} = S_{33}^{(1)} = 0 \\
S_{11}^{(2)} &= 32r\left(3-7v_0+4v_0^2\right) + 3\pi\mu_0\,(\alpha+\beta)\,, \\
S_{22}^{(2)} &= S_{12}^{(2)} = S_{21}^{(2)} = S_{11}^{(2)} \\
S_{13}^{(2)} &= 4\,(1-v_0)^2\,(16r+3\pi\mu_0\alpha)\,, \\
S_{23}^{(2)} &= S_{31}^{(2)} = S_{32}^{(2)} = S_{13}^{(2)},\ S_{33}^{(2)} = 0
\end{aligned} \tag{6}$$

where r is the radius of the fiber; λ_0, μ_0 and ν_0 are the Láme constant, shear modulus, and Poisson's ratio of the matrix, respectively. $\mathbf{S}_2$ and $\mathbf{S}_3$ in Eq. (2) denote the Eshelby's tensor for the debonded cylindrical fiber (phase 2) and the spherical micro-crack void (phase 3), and their components are given in "Appendix 1".

By carrying out lengthy algebra, the stiffness tensor for the four-phase composite containing UD fiber can be derived, and takes the following form:

$$\mathbf{C}^* = C_{IK}^{(1)}\delta_{ij}\delta_{kl} + C_{IJ}^{(2)}\left(\delta_{ik}\delta_{jl}+\delta_{il}\delta_{jk}\right) \tag{7}$$

in which

$$\begin{aligned}
C_{IK}^{(1)} &= 2\lambda_0 F_{KK}^{(2)} + 2\mu_0 F_{IK}^{(1)} + \lambda_0\sum_{R=1}^{3} F_{RK}^{(1)}, \\
C_{IJ}^{(2)} &= \mu_0\left(F_{IJ}^{(2)} + F_{JI}^{(2)}\right)
\end{aligned} \tag{8}$$

where the parameters ${F_{IK}}^{(1)}$ and ${F_{IJ}}^{(2)}$ are listed in "Appendix 2". Based on the derived stiffness tensor ${C_{IK}}^{(1)}$ and ${C_{IJ}}^{(2)}$, the five effective elastic moduli for continuous fibrous composites along the fiber axis can be recast as [9,21]

$$E_A^* = C_{33}^{(1)} + 2C_{33}^{(2)} - \frac{\left(C_{13}^{(1)}\right)^2}{C_{11}^{(1)}+C_{11}^{(2)}},\ v_A^* = \frac{C_{13}^{(1)}}{2\left(C_{11}^{(1)}+C_{11}^{(2)}\right)}$$

$$\kappa_T^* = C_{11}^{(1)} + C_{11}^{(2)},\ \mu_T^* = C_{11}^{(2)},\quad \mu_A^* = C_{13}^{(2)}, \tag{9}$$

where E, v, κ, and μ are, respectively, the Young's modulus, Poisson's ratio, bulk modulus, and shear modulus; the subscripts A and T signify the axial and transverse directions [21]. The transverse Young's modulus and Poisson's ratio can also derived from Eq. (9) as

$$E_T^* = \frac{4\kappa_T^*\mu_T^*}{\kappa_T^*+\Upsilon\mu_T^*},\quad v_T^* = \frac{\kappa_T^*-\Upsilon\mu_T^*}{\kappa_T^*+\Upsilon\mu_T^*} \tag{10}$$

with

$$\Upsilon = 1 + \frac{4\left(v_A^*\right)^2\kappa_T^*}{E_A^*} \tag{11}$$

Furthermore, based on the governing equation for the UD fiber-reinforced composites, in conjunction with the transformation law [22], the following stress–strain transformations through an angle θ along 1-axis can be derived as [16,23]

$$\boldsymbol{\sigma}_\varsigma = \mathbf{T}_1^{-1}\cdot\mathbf{C}\cdot\mathbf{T}_2 : \boldsymbol{\varepsilon}_\xi \equiv C\,(\boldsymbol{\theta}) : \boldsymbol{\varepsilon}_\xi \tag{12}$$

with

$$\mathbf{T}_1 = \begin{bmatrix}
\cos^2\theta & 0 & \sin^2\theta & 0 & -2\cos\theta\sin\theta & 0 \\
0 & 1 & 0 & 0 & 0 & 0 \\
\sin^2\theta & 0 & \cos^2\theta & 0 & 2\cos\theta\sin\theta & 0 \\
0 & 0 & 0 & \cos\theta & 0 & \sin\theta \\
\cos\theta\sin\theta & 0 & -\cos\theta\sin\theta & 0 & \cos^2\theta-\sin^2\theta & 0 \\
0 & 0 & 0 & -\sin\theta & 0 & \cos\theta
\end{bmatrix},$$

$$\mathbf{T}_2 = \begin{bmatrix}
\cos^2\theta & 0 & \sin^2\theta & 0 & -\cos\theta\sin\theta & 0 \\
0 & 1 & 0 & 0 & 0 & 0 \\
\sin^2\theta & 0 & \cos^2\theta & 0 & \cos\theta\sin\theta & 0 \\
0 & 0 & 0 & \cos\theta & 0 & \sin\theta \\
2\cos\theta\sin\theta & 0 & -2\cos\theta\sin\theta & 0 & \cos^2\theta-\sin^2\theta & 0 \\
0 & 0 & 0 & -\sin\theta & 0 & \cos\theta
\end{bmatrix} \tag{13}$$

In accordance with the aforementioned process, the effective stiffness matrix of the fibrous composites considering the fiber orientation (θ) can be explicitly written as

$$\mathbf{C}(\boldsymbol{\theta}) = \begin{bmatrix}
\bar{C}_{11} & \bar{C}_{12} & \bar{C}_{13} & 0 & \bar{C}_{15} & 0 \\
\bar{C}_{21} & \bar{C}_{22} & \bar{C}_{23} & 0 & \bar{C}_{25} & 0 \\
\bar{C}_{31} & \bar{C}_{32} & \bar{C}_{33} & 0 & \bar{C}_{35} & 0 \\
0 & 0 & 0 & \bar{C}_{44} & 0 & \bar{C}_{46} \\
\bar{C}_{51} & \bar{C}_{52} & \bar{C}_{53} & 0 & \bar{C}_{55} & 0 \\
0 & 0 & 0 & \bar{C}_{64} & 0 & \bar{C}_{66}
\end{bmatrix} \tag{14}$$

where the parameters $\bar{c}_{ij}$ $(i,\,j=1{-}6)$ in Eq. (14) are listed in "Appendix 3".

2.2 Debonding damage and micro-crack modeling

In the present study, interfacial debonding and micro-cracks were chosen as the major factors impacting the failure mechanism in composites, and these were included in the present analytical constitutive model for a more precise prediction. Following [10], a damage model based on the Weibull probability distribution function [24] was considered to describe the evolutionary interfacial debonding between the matrix and fibers [10]. The debonding damage can be modeled as the volume fraction of the debonded fiber ϕ_2, which can be expressed as [24–26]

$$\phi_2 = \phi \left\{ 1 - \exp\left[-\left(\frac{(\boldsymbol{\sigma}_f)^a}{S_0} \right)^M \right] \right\} \tag{15}$$

where ϕ denotes the original (initial) volume fraction of fiber; S_0 and M are the Weibull probability parameters, which are related to the interfacial strength and progressive rate of debonding damage, respectively [11]. Following the numerical analysis of the debonding parameter reported in [11], the Weibull probability parameter of interfacial strength, denoted by S_0, is defined as $S_0 = S \cdot \sigma_y$, where σ_y is the yield stress of the composite. Moreover, $(\boldsymbol{\sigma}_f)^a$ signifies the averaged internal stress of fibers induced by external loading and/or deformations, explicitly derived as [16]

$$\begin{aligned} \boldsymbol{\sigma}_f = {} & \mathbf{C}_1 \cdot \left[\mathbf{I} - \mathbf{S}_1 \cdot (\mathbf{A}_1 + \mathbf{S}_1)^{-1} \right] \\ & \cdot \left[\mathbf{I} - \phi_1 \mathbf{S}_1 \cdot (\mathbf{A}_1 + \mathbf{S}_1)^{-1} \right]^{-1} : \bar{\boldsymbol{\varepsilon}} \equiv \mathbf{U} : \bar{\boldsymbol{\varepsilon}} \end{aligned} \tag{16}$$

in which

$$U_{ijkl} = U_{IK}^{(1)} \delta_{ij}\delta_{kl} + 2U_{IJ}^{(2)} \left(\delta_{ik}\delta_{jl} + \delta_{il}\delta_{jk} \right) \tag{17}$$

with

$$\begin{aligned} U_{IK}^{(1)} &= 2\lambda_1 \xi_{KK}^{(2)} + 2\mu_1 \xi_{IK}^{(1)} + \lambda_1 \sum_{R=1}^{3} \xi_{RK}^{(1)}, \\ U_{IJ}^{(2)} &= \mu_1 \left(\xi_{IJ}^{(2)} + \xi_{JI}^{(2)} \right) \end{aligned} \tag{18}$$

where λ_1 and μ_1 are the Láme constant and shear modulus of fiber, and the parameters ${\xi_{IK}}^{(1)}$ and ${\xi_{IJ}}^{(2)}$ can be defined as follows:

$$\begin{aligned} \xi_{IK}^{(1)} &= \frac{1}{2} \left(\frac{-P_{IK}^{(1)}}{D_{KK}^{(2)}} + \frac{\chi_{IK} \left(2P_{II}^{(2)} - 1 \right)}{D_{II}^{(2)}} \right) + \sum_{R=1}^{3} \frac{P_{IR}^{(1)} \chi_{RK}}{2D_{RR}^{(2)}}, \\ \xi_{IJ}^{(2)} &= \frac{1}{4} \left(\frac{1}{2} - P_{IJ}^{(2)} \right) \left(\frac{1}{D_{IJ}^{(2)}} + \frac{1}{D_{JI}^{(2)}} \right) \end{aligned} \tag{19}$$

with

$$\begin{Bmatrix} \chi_{I1} \\ \chi_{I2} \\ \chi_{I3} \end{Bmatrix} = \begin{bmatrix} D_{11}^{(1)} + 2D_{11}^{(2)} & D_{21}^{(1)} & D_{31}^{(1)} \\ D_{12}^{(1)} & D_{22}^{(1)} + 2D_{22}^{(2)} & D_{32}^{(1)} \\ D_{13}^{(1)} & D_{23}^{(1)} & D_{33}^{(1)} + 2D_{33}^{(2)} \end{bmatrix}^{-1} \begin{Bmatrix} D_{I1}^{(1)} \\ D_{I2}^{(1)} \\ D_{I3}^{(1)} \end{Bmatrix} \tag{20}$$

and

$$D_{IK}^{(1)} = -\phi_1 P_{IK}^{(1)}, \quad D_{IJ}^{(2)} = \frac{1}{2} - \phi_1 P_{IJ}^{(2)} \tag{21}$$

where the parameters ${P_{IK}}^{(1)}$ and ${P_{IJ}}^{(2)}$ are given in Eq. (34) of "Appendix 2". From the derived internal stress of the fiber $(\boldsymbol{\sigma}_f)$ through Eqs. (16)–(21), the averaged internal stresses of UD fibers, $(\boldsymbol{\sigma}_f)^a$, in composites can be calculated as

$$\begin{aligned} & (\boldsymbol{\sigma}_f)^a \\ & = \sqrt{(\boldsymbol{\sigma}_f)_{11}^2 + (\boldsymbol{\sigma}_f)_{22}^2 + (\boldsymbol{\sigma}_f)_{33}^2 + 2\left((\boldsymbol{\sigma}_f)_{23}^2 + (\boldsymbol{\sigma}_f)_{13}^2 + (\boldsymbol{\sigma}_f)_{12}^2 \right)} \end{aligned} \tag{22}$$

Furthermore, the nucleation of spherical micro-crack density in composites by external loading and deformations is modeled here in accordance with the continuum damage model [14,15], as follows

$$\phi_3 = \begin{cases} \phi_{initial} \\ \phi_{initial} + c_1 \left(1 - \frac{\varepsilon^{th}}{\varepsilon^a} \right)^{c_2} \end{cases} \tag{23}$$

where $\phi_{initial}$ and ε^{th} signify the initial density of micro-cracks and the strain threshold below which no nucleation occurs [16]. c_1 and c_2 are the micro-croak parameters, which are related to the intensity and distribution of micro-crack nucleation, respectively. In addition, ε^a is the current effective macroscopic strain in composites, which can be defined as [15]

$$\varepsilon^a = \sqrt{\varepsilon_{11}^2 + \varepsilon_{22}^2 + \varepsilon_{33}^2 + 2\left(\varepsilon_{23}^2 + \varepsilon_{13}^2 + \varepsilon_{12}^2 \right)} \tag{24}$$

Overall, the material damage modeling presented here includes seven model parameters. These are related to the fiber interface (α and β), debonding damage (S_0 and M), and micro-crack (ε^{th}, c_1, and c_2) characteristics. These parameters need to be properly estimated since they can have a significant effect on the overall predictions for the composites. However, it is not guaranteed that estimating the optimal parameter set manually will provide the most reasonable solution. The evolutionary computation method-based GA is thus applied in the present study to find the optimal combination of parameters in the derived model.

Table 1 Procedure for optimizing parameter sets in the constitutive equation using genetic algorithm

Step 1: Generate the initial population of chromosomes

$$P_{set} = [\sigma_\theta, \sigma_\varphi, K, S_0, M, \varepsilon^{\text{th}}, c_1, c_2]$$

while satisfaction of stopping criteria **OR** number of generation is less than the maximum number of generation ($N_{\max\_gen}$)

Step 2: Evaluate the penalty of each chromosome ($\hat{D}_i$: estimated strain values at the i-th chromosome, D: experimental results)

$$F_{penalty} = \arg\min_{\hat{P}_{set}} \sum_{i=1}^{N_{\max\_gen}} \left(\hat{D}_i - D\right)^T \left(\hat{D}_i - D\right)$$

Step 3: Select the best chromosome and perform reproduction

Step 4: Perform crossover and mutation

end

Step 5: Achieve the best individual in all generation

2.3 Application of genetic algorithm

In this paper, the GA, an evolutionary computation method is used to find the optimal parameter sets in the proposed constitutive equation. The GA introduced by Fraser [27] is guaranteed to converge to an optimal solution in a multivariable function by repeating population generation, fitness/penalty evaluation, selection, reproduction, crossover, and mutation [27,28]. Compared to other optimization methods, it is capable of solving any optimization problem based on a chromosome approach and is capable of handling multiple solution search space with less complexity and while being more straightforward [29].

The entire procedure for optimizing the parameter sets of the constitutive equation by using the GA is shown in Table 1. As shown in the table, the initially generated population of chromosomes, composed of parameters of the proposed constitutive equation of fibrous composites such as $P_{set} = [\sigma_\theta, \sigma_\varphi, K, S, M, \varepsilon^{\text{th}}, c_1, c_2]$, is generated. Here, σ_θ, σ_φ, K, S, M, ε^{th}, c_1, and c_2 denote the fiber angle, volume fraction of fiber, scale factor of fiber interface, interfacial strength, progressive rate of debonding damage, strain threshold of micro-crack, micro-crack intensity, and distribution of micro-crack nucleation, respectively. To reflect the uncertainties in the experiments and human-induced error, σ_θ and σ_φ are included in the parameter set with a range of $[-3, 3]$ deg at an interval of 0.1 and $[-0.01, 0.01]$ at an interval of 0.001, respectively.

After being generated, each chromosome is evaluated in terms of the penalty and best chromosome, which minimizes the difference between the estimated and previously obtained stress values. The chromosome with the lowest penalty value has a higher probability of being selected in the next generation. The selected best chromosome is reproduced to form a new population, and crossover and mutation are performed to prevent the GA from converging on a local minimum. Based on the updated population, Steps 2–4 are looped until the stopping criterion is satisfied or the number of generations reaches the maximum number of generations. The parameter set with the minimum penalty value is selected and the constitutive equation is automatically tuned.

3 Numerical simulations

A comprehensive numerical simulation is carried out in this section to illustrate the influence of the model parameters on the effective properties of the composite. For convenience, the material properties for AS4 carbon fiber-reinforced polyether ether ketone (PEEK) composites used in [30] are adopted as follows: $E_m = 6.14$ GPa, $\upsilon_m = 0.356$; $E_f = 214$ GPa, $\upsilon_f = 0.263$, $\phi_f = 60\%$; $\sigma_y = 150$ MPa, where the subscripts m and f signify the matrix and fiber, respectively.

Based on the above material constants, predictions with various typical values for the model parameters are depicted

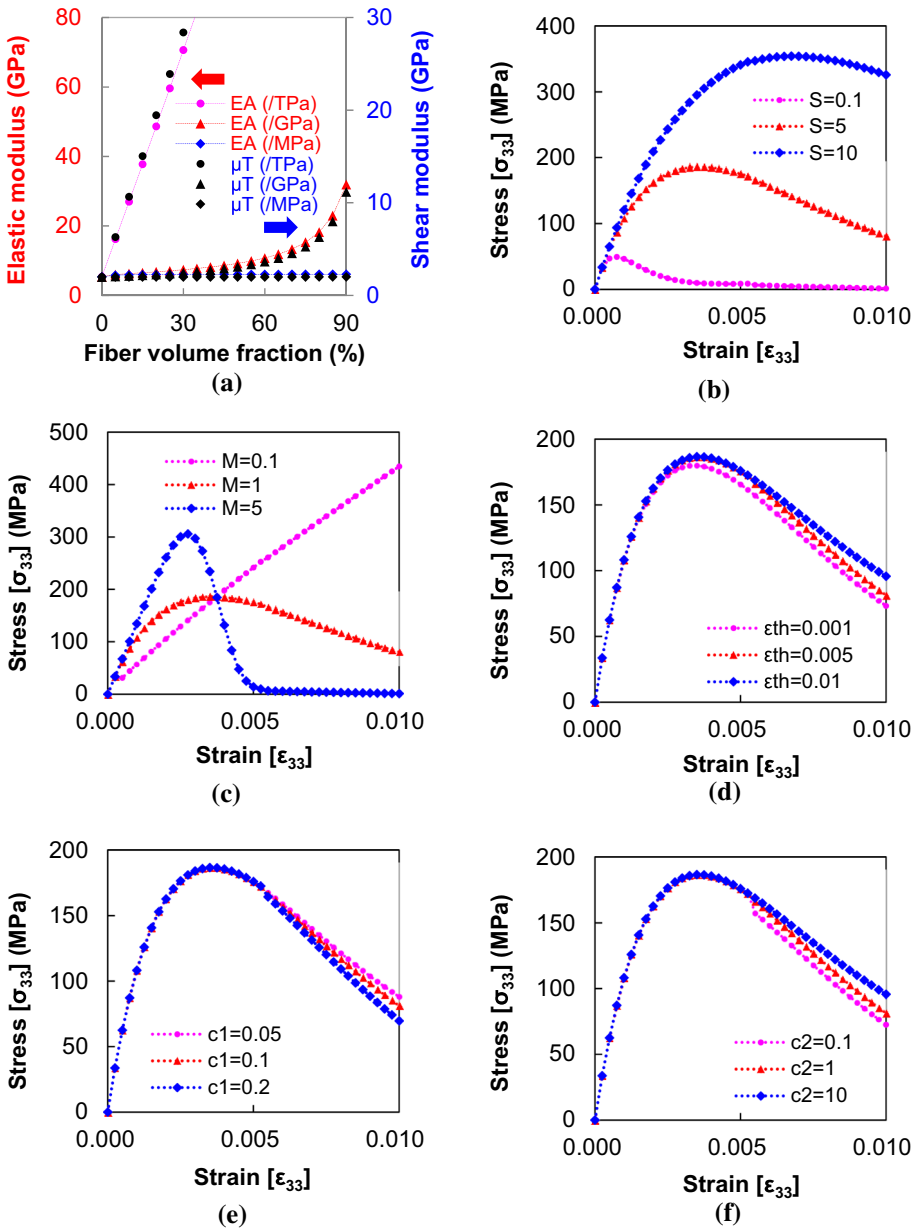

Fig. 3 The predicted mechanical behaviors of AS4 carbon fiber-reinforced PEEK composites with various model parameters

in Fig. 3. Figure 3a displays the predicted effective axial Young's and transverse shear moduli of the composite to illustrate the effects of the interface characteristics (K) between the matrix and fibers. As shown in the figure, the properties of the effective mechanical constants are reduced when the scale of the interface parameter that is defined as K decreases. It should also be noted that interface characteristics tend to be emphasized when the volume fraction of the fibers increases.

To investigate the effects of debonding damage on the stress–strain behaviors of composites, numerical tests of S and M were carried out, and the results are shown in Fig. 3b, c. The nonlinear responses (concave downwards) that occur with different model parameters in Fig. 3b, illustrate that the resistance to debonding damage grows when the interfacial strength S increases. Figure 3c shows that a higher value of M, which is associated with the rate of progressive debonding damage, leads to a faster evolution of interfacial debonding.

The present method-based predictions with varying model parameters for micro-cracks (ε^{th}, c_1 and c_2), exhibited in Fig. 3d–f, were further investigated to determine how micro-crack damage influences the mechanical and toughness behaviors of composites. It is predicted in Fig. 3d that the micro-crack effect is more pronounced at a lower strain threshold of micro-crack nucleation (ε^{th}). Figure 3d clearly shows that the toughness on the energy absorption of composites is associated with the initial threshold of micro-cracks within the matrix.

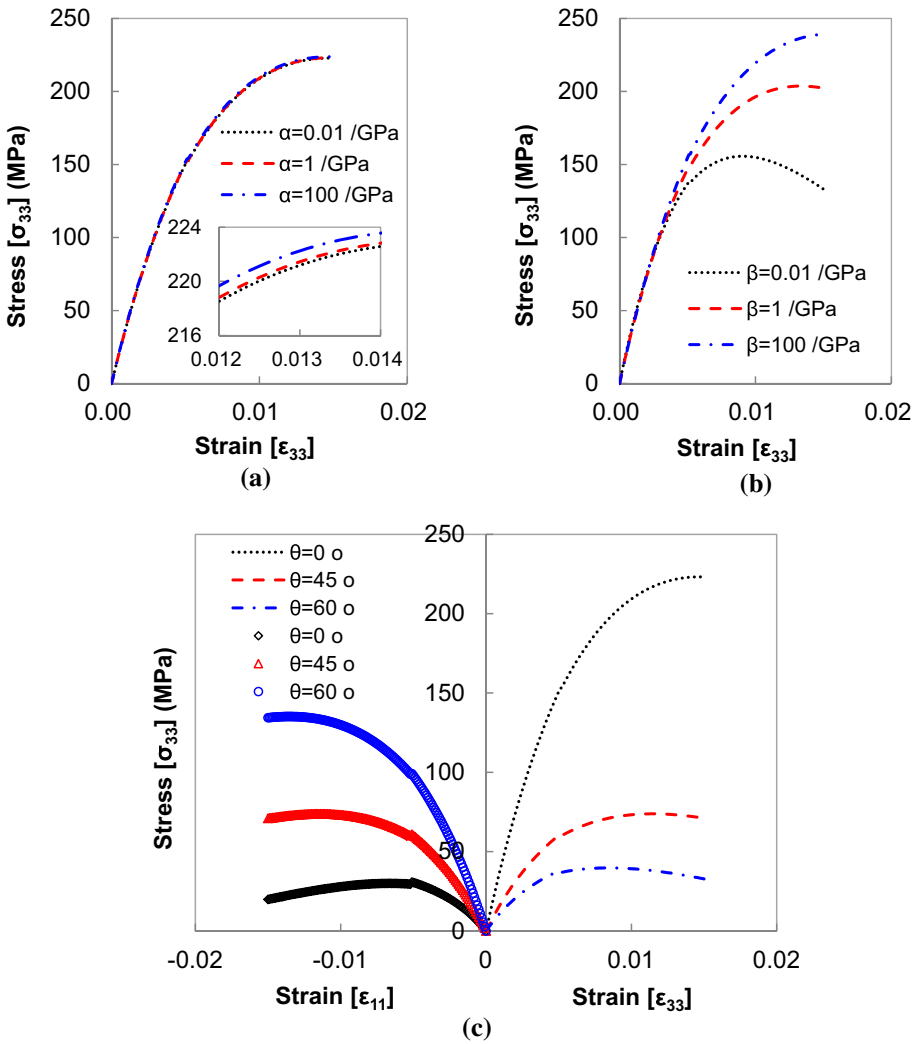

Fig. 4 The predicted stress–strain responses of E-glass fiber-reinforced epoxy composites under uniaxial tensile loading with various interface parameters of **a** the tangential, α, and **b** normal, β, components of compliance, and **c** under biaxial tensile loading with respect to fiber direction, θ

Various values of the micro-crack parameters c_1 and c_2, which are related to the intensity and distribution of micro-crack nucleation, are shown in Fig. 3e, f, respectively. As displayed in Fig. 3e, reduced stiffness appears at a later strain range as the micro-crack parameter c_1 increases. In contrast, as the parameter value c_2 increases from 0.1 to 10, higher effective stress–strain responses are predicted. It is also observed from Fig. 3f that the effect of the second micro-crack parameter c_2 is more influential on the stress–strain behavior of the composites than the first micro-crack parameter c_1.

To further illustrate the descriptive with respect to the model parameters in the proposed model, an additional numerical simulation of E-glass fiber-reinforced epoxy composites was carried out. The adopted material constants are [31]: $E_m = 2.6\,\text{GPa}$, $v_m = 0.4$; $E_f = 72.5\,\text{GPa}$, $v_f = 0.22$. The influence of the interface scale (K) on the elastic behavior of the composites is investigated in Fig. 3, and additional parametric studies of the compliance parameters in the tangential (α) and normal (β) directions of the interface are illustrated in Fig. 4a, b, respectively. In the figures, stiffer behaviors are predicted as the values of both interface constants are increased, and the effect of β is more influential than that of α.

The fiber orientation in composite materials is also a very important factor in composite design, and is known to have a great effect on the material/structural behaviors under multi-axial loading conditions. The biaxial stress–strain responses for various fiber angles ($0°, 45°, 60°$) consequently calculated, and are shown in Fig. 4c. Stiffer stress–strain responses in the 3–3 axis are obtained when the fiber orientation angle is small, but inversely proportional to this, weak behaviors in the 1–1 axis are predicted as the orientation degree decreases. When the orientation angle is 45°, the 1 and 3 axis behaviors are predicted to be similar under biaxial tensile loading conditions.

The micromechanical model employed here is based on the EVA method proposed by Ju et al. [6,7]. In the EVA approach, instead of estimating the exact local solution of the fiber interaction problem, a simple but accurate approximate

analytical solution has been derived to predict the effective behaviors of multi-phase composites [7]. Because of the non-interacting approximation for mathematical simplicity, the proposed model may be limited when predicting high volume fraction fiber-reinforced composites [32]. However, in the present study, we tried to overcome this limitation by applying various additional mechanisms, such as interface and microcracks, to the classical EVA model.

A comparison with the finite element (FE) calculation [31] was carried out for validation purpose. An E-glass fiber-reinforced epoxy composites $[0/90_3/0]_T$ with 52.5% volume fraction is considered here; the subscripts 3 and T denote the number of layers and total, respectively. The material constants are [31]: $E_m = 2.6\,\text{GPa}$, $v_m = 0.4$; $E_f = 72.5\,\text{GPa}$, $v_f = 0.22$. The effective constitutive equation of the cross-ply laminate composite can be explicitly calculated by substituting the proposed model into the laminate theory as [22,33]

$$\begin{Bmatrix} N \\ M \end{Bmatrix} = \begin{bmatrix} A & B \\ B & D \end{bmatrix} \begin{Bmatrix} \varepsilon^0 \\ \kappa \end{Bmatrix} \tag{25}$$

where $\{N\}$ and $\{M\}$ denote the inplane forces and moments, respectively; $\{\varepsilon^0\}$ and $\{\kappa\}$ are the midplane strains and curvatures of the laminate composites. The coefficients $[A]$ through $[D]$ are defined as [22]

$$\begin{aligned} [A] &= \sum_{k=1}^{n} [C(\theta)](z_k - z_{k-1}), \\ [B] &= \frac{1}{2}\sum_{k=1}^{n} [C(\theta)]\left(z_k^2 - z_{k-1}^2\right), \\ [D] &= \frac{1}{3}\sum_{k=1}^{n} [C(\theta)]\left(z_k^3 - z_{k-1}^3\right) \end{aligned} \tag{26}$$

where z signifies the integrated over the laminate thickness, k denotes the individual number of layer, and the matrix $C(\theta)$ is given in Eq. (14). As shown in Fig. 5, the present prediction is quantitatively a good match with the FE result and the experimental data without the GA calibration process.

The present numerical simulations in this section provide the upper and lower bounds of the model parameters in the proposed framework. In conjunction with previous related works [9–11,13,15], the ranges of each parameter for optimal set estimation by the GA are: $\alpha = 2K$ and $\beta = 3K$, where $K = 10^{-6}-10^{6}/\text{Pa}$ and the increment is 10; $S = 0.1-10$ and $M = 0.1-5$, where the increment is 0.01; $\varepsilon^{\text{th}} = 0.001-0.1$, where the increment is 0.001; $c_1 = 0.001-0.2$, where the increment is 0.001; and $c_2 = 0.1-10$, where the increment is 0.1. In this study with the GA, a single point crossover, stochastic uniform selection, and a Gaussian mutation operator are used. Percent

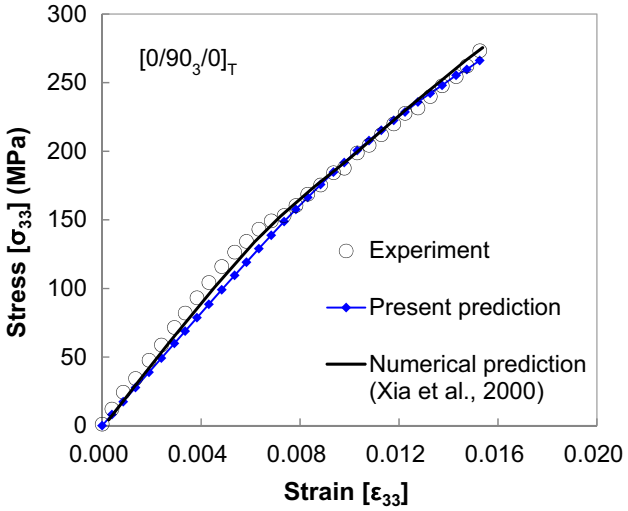

Fig. 5 Comparisons of the prediction values, experimental results, and numerical predictions of the uniaxial tensile responses of E-glass fiber reinforced epoxy matrix composites

probability of crossover of 0.6, maximum number of generations of 150, and stall generation of 100 with the average relative change in 1e−6 are used.

4 Validation of the proposed approach

To assess the predictive capability of the proposed approach, comparisons were made between the predictions for various composite systems and previous experimental results [18,30,31,34–37]. The micromechanics-based formulation developed here is coupled with the GA, and the optimal set of model parameters is estimated by comparing it with the experimental data. We first conduct a convergence study of population size with GA to obtain a reasonable population scale, which is essential in developing a reliable simulation.

In most GA simulations, the prediction reliability is improved as the population size increases, while the computational cost increases in inverse proportion to the population size. We consider five different sizes of population and compare the estimated strain values with the experimental data obtained by Weeks and Sun [30]. Figure 6 shows the calculated the normalized root mean square error (NRMSE) and normalized computational cost (NCC) with different levels of population. It can be concluded from Fig. 6 that the influence of population size on the NRMSE is negligible beyond a population size of 50. NCC, however, exponentially increased with an increase in the population size, indicating that a reasonable population size is required for an accurate and efficient simulation. In this study, a population size of 50 is determined by test results, as shown in Fig. 6.

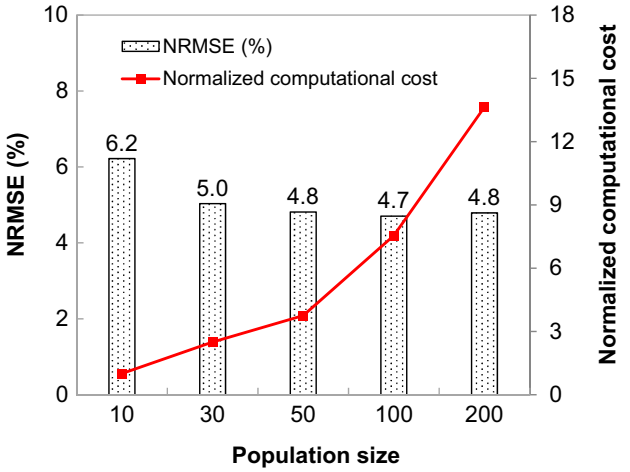

Fig. 6 The calculated NRMSE and normalized computational cost based on the present GA simulation

4.1 Comparative study between experimentally measured moduli and present predictions

The results of a comparative study of effective longitudinal Young's modulus (E_A), transverse Young's modulus (E_T), and transverse shear modulus (μ_T) of graphite (AS) fiber-reinforced epoxy (3501) composites [18] are shown in Fig. 7. We employ the material properties of the composites as follows [18]: $E_m = 5.35\,\text{GPa}$, $\upsilon_m = 0.35$; $E_f = 232\,\text{GPa}$, $\upsilon_f = 0.22$. Since the stress–strain curve of the composites is not reported by Huang [18], only the interface parameters of the proposed framework are estimated by the GA approach with a population size of 50. The calculated interface parameters are: $\alpha = 2 \times 10^{-3}$ and $\beta = 3 \times 10^{-3}$/MPa.

Figure 7a shows a comparison between the experimental data [18] and the present prediction based on the above model and material parameters. Overall, it can be seen from the figure that the experimental results and the present prediction match well. The calculated representative penalty values by the GA corresponding to Fig. 7a are depicted in Fig. 7b. In this figure, the black squares signify the mean penalty value, while the blue dots represent the mean penalty value. It can be seen that as the population size continues to increase, the best penalty value converge, reaching a state of equilibrium.

4.2 Uniaxial and transverse tensile tests and present predictions

To further investigate the applicability of the present combined analytical and numerical formulation, the prediction by the proposed approach is compared with (1) a uniaxial tensile test of silicon carbide (SCS) fiber-reinforced calcium aluminosilicate composites [35] and (2) a transverse tensile test of SCS-6 fiber/Ti-6 composites [36]. Following

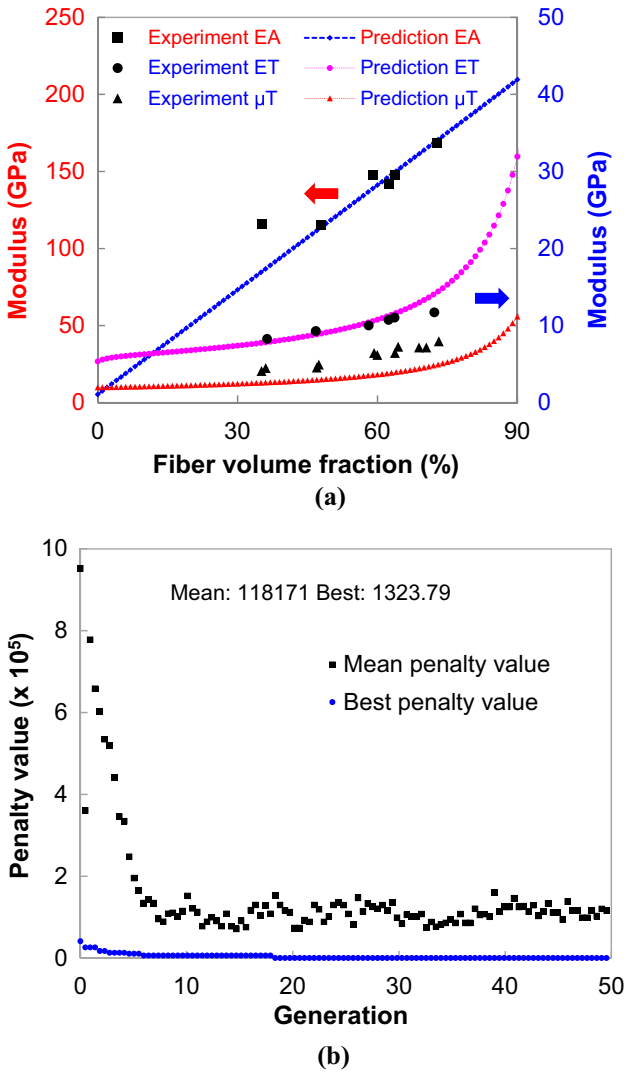

Fig. 7 **a** Comparisons of the predicted longitudinal Young's modulus, transverse Young's modulus, and transverse shear modulus of graphite (AS) fiber-reinforced epoxy (3501) composites and **b** the representative penalty values calculated by the GA corresponding to **a**

[35], we adopt the material properties of the SCS/calcium aluminosilicate composites as follows: $E_m = 97.9\,\text{GPa}$, $\upsilon_m = 0.25$; $E_f = 188\,\text{GPa}$, $\upsilon_f = 0.3$, $\sigma_y = 320\,\text{MPa}$, $\phi_y = 36\%$. The model parameters are estimated by GA as: $\alpha = 2 \times 10^{-1}$ /MPa, $\beta = 3 \times 10^{-1}$/MPa, $S = 3.96$, $M = 1.75$, $\varepsilon^{\text{th}} = 0.002$, $c_1 = 0.2$, $c_2 = 0.4$. In addition, the adopted material and model parameters for simulation of SCS-6 fiber/Ti-6 composites [36] are: $E_m = 120\,\text{GPa}$, $\upsilon_m = 0.31$; $E_f = 393\,\text{GPa}$, $\upsilon_f = 0.25$, $\sigma_y = 370\,\text{MPa}$, $\phi_y = 45\%$; $\alpha = 2 \times 10^{-5}$/MPa, $\beta = 3 \times 10^{-5}$/MPa, $S = 0.4$, $M = 1.25$, $\varepsilon^{\text{th}} = 0.003$, $c_1 = 0.2$, $c_2 = 7.5$.

As illustrated in Fig. 8a, b, the present predicted stress–strain responses match well with both experimental data for composites under uniaxial and transverse tensile loading. The theoretical predictions on the volume fraction of fiber rein-

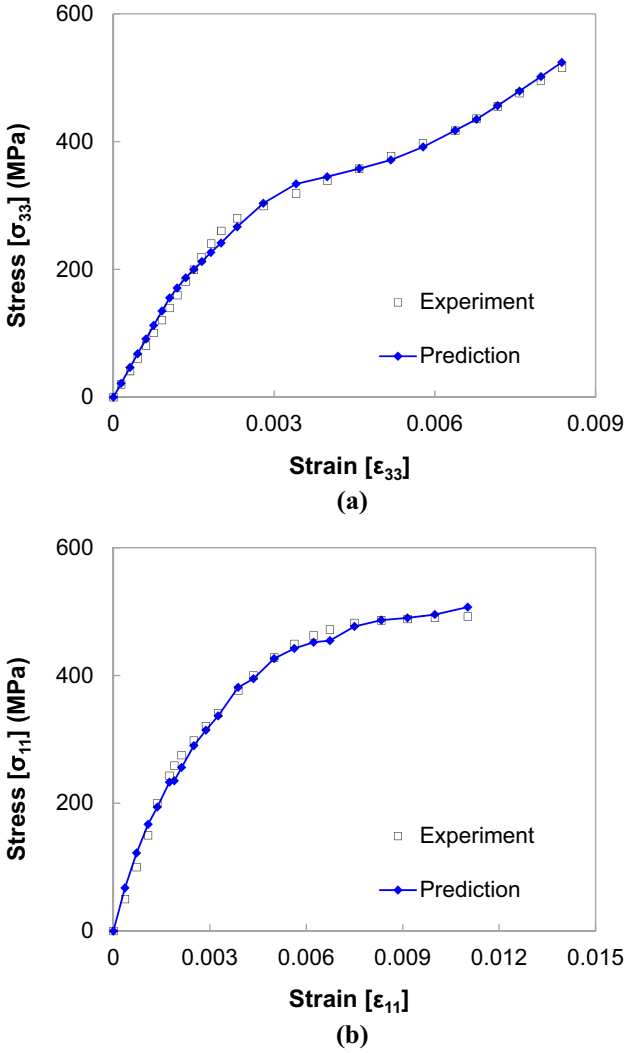

Fig. 8 Comparisons of present predicted stress–strain curves of fibrous composites under **a** uniaxial and **b** transverse tensile loadings

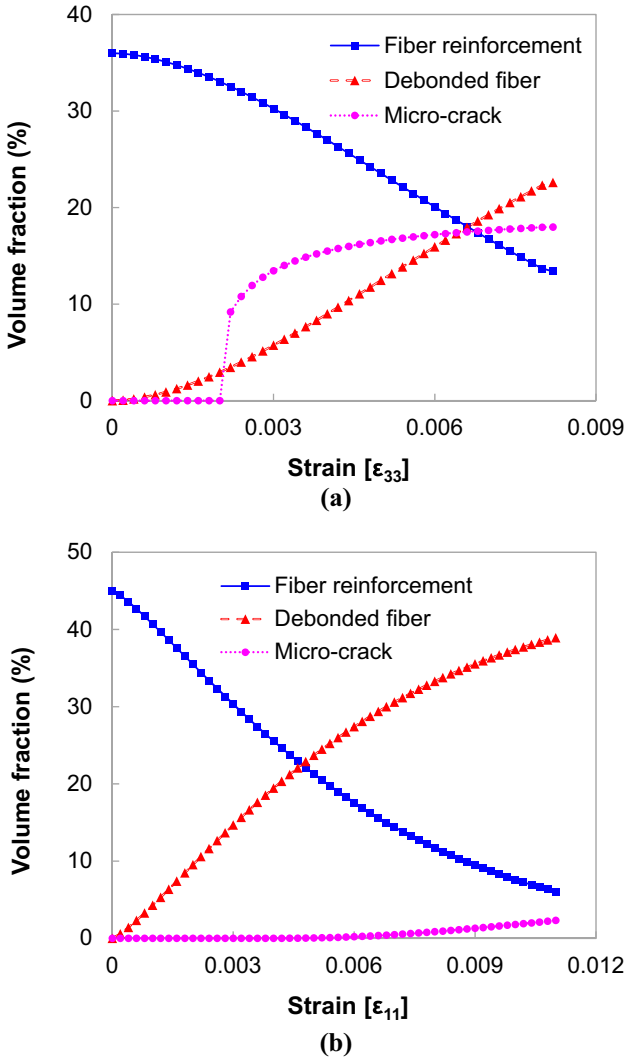

Fig. 9 The theoretical predictions of the volume fraction of fiber reinforcement, debonded fiber and micro-crack under **a** uniaxial and **b** transverse tensile loading corresponding to Fig. 8a, b, respectively

forcement, debonded fiber, and micro-cracks under uniaxial and transverse tensile loadings corresponding to Fig. 8a, b are depicted in Fig. 9a, b, respectively. Interestingly, it is observed that the predicted damage patterns and progressions by the proposed approach with the GA depend strongly on the loading conditions, illustrating realistic damage responses. When uniaxial tensile loading is applied to the composites, the debonding damage between the matrix and fibers evolves smoothly, whereas a micro-crack occurs suddenly and significantly (Fig. 9a). However, as observed from Fig. 9b, the opposite trends to the previous case are predicted under transverse tensile loading.

4.3 Comparative study with multiple experimental test results

Herakovich [34] investigated the transverse tensile stress–strain behaviors of a continuous BP–SiC fiber-reinforced Ti–6Al–4V matrix composite, and reported multiple test results. We adopt the material properties of the composites as follows [34]: $E_m = 110\,\text{GPa}$, $\upsilon_m = 0.33$; $E_f = 390\,\text{GPa}$, $\upsilon_f = 0.19$, $\sigma_y = 370\,\text{MPa}$, $\phi_y = 34\%$. The estimated model parameters based on the GA are: $\alpha = 2 \times 10^{-6}/\text{MPa}$, $\beta = 3 \times 10^{-6}/\text{MPa}$, $S = 0.86$, $M = 1.05$, $\varepsilon^{\text{th}} = 0.004$, $c_1 = 0.126$, $c_2 = 2.6$. The comparison of the stress–strain curves between present a theoretical prediction and various experimental data for the same material composition [34] are represented in Fig. 10a and the corresponding damage evolution curves are given in Fig. 10b. Similar to the previous comparisons, the predicted stress–strain behaviors and damage trends are in good agreement with the experimental data. Note that the unsmoothed curves in Figs. 8, 9 and 10 are due to characteristics of the present GA method. Each experimen-

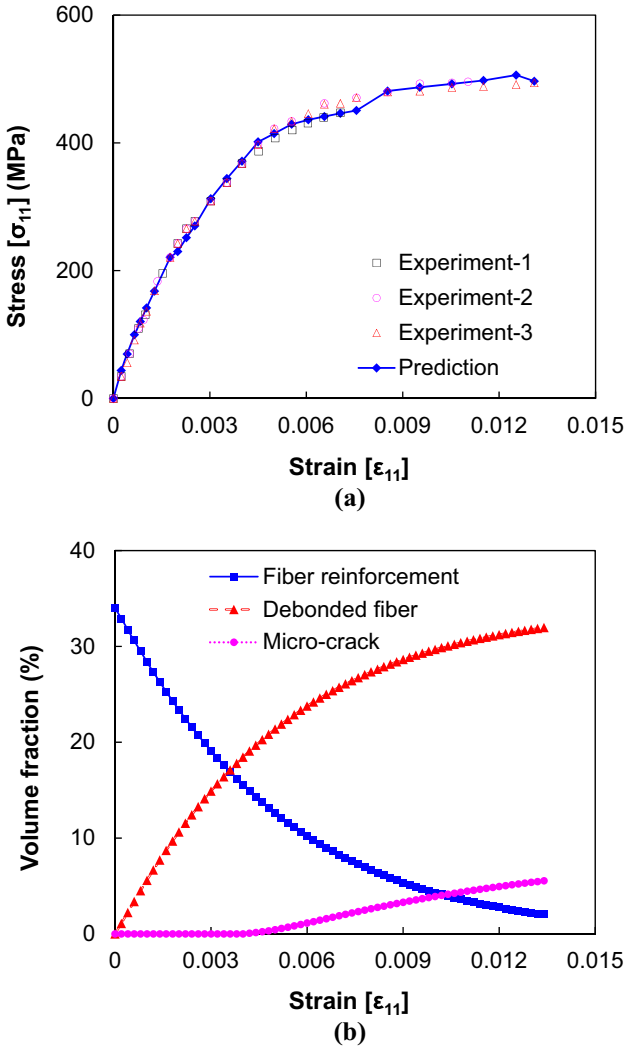

Fig. 10 **a** Comparison of stress–strain curves between present theoretical prediction and various experimental data for the same material composition and **b** the corresponding damage evolution curves

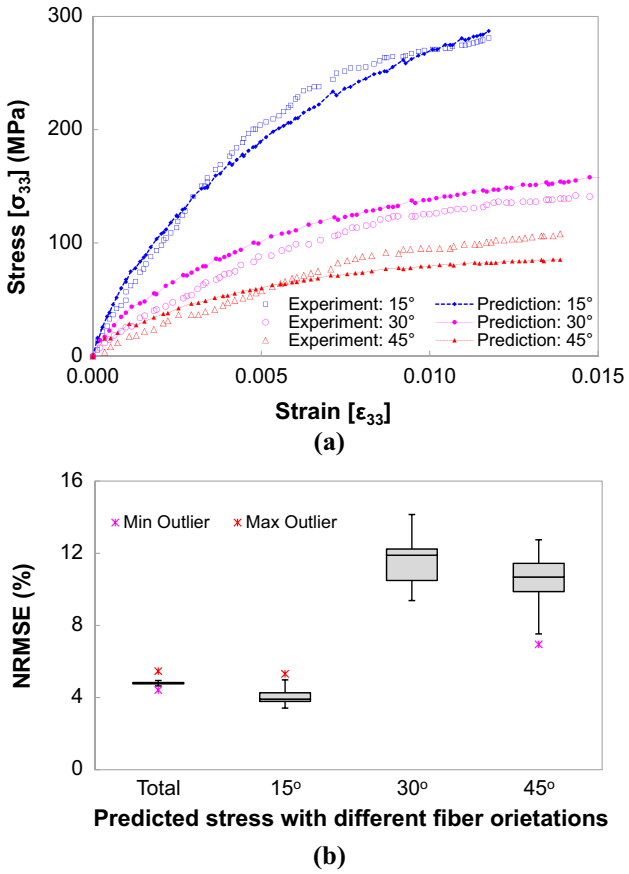

Fig. 11 **a** Experimental comparisons with the present predictions of AS4 carbon fiber/PEEK composites with various fiber orientations (θ) and **b** *boxplots* of 100 Monte Carlo simulation results of the corresponding NRMSE calculated via GA

tal result of stress–strain coordinates is programmed for a 1:1 comparison with the corresponding simulated predictions.

We further compare the present predictions based on the proposed framework with multiple experimental test results of PEEK composites containing different orientations of AS4 carbon fiber [30]. The material properties and estimated model parameters are as follows: $E_m = 6.14\,\text{GPa}$, $\upsilon_m = 0.356$; $E_f = 214\,\text{GPa}$, $\upsilon_f = 0.263$, $\sigma_y = 150\,\text{MPa}$, $\phi_y = 60\,\%$; $\alpha = 2/\text{MPa}$, $\beta = 3/\text{MPa}$, $S = 5.51$, $M = 0.37$, $\varepsilon^{\text{th}} = 0.001$, $c_1 = 0.157$, $c_2 = 0.1$. Figure 11a shows the experimental comparison results, indicating that there is a good correlation between the experimental data and the predictions considering various fiber orientations.

The performance of the proposed analytical model integrated with the GA is analyzed statistically with a Monte Carlo simulation (MCS) by randomly generating an initial population of the chromosome. Boxplots of 100 MCS results are shown in Fig. 11b. As shown in the figure, the estimated strain values are in good agreement with the experimental results with less than 14.14% of NRMSE, indicating the predictive capability of the proposed analytical model integrated with the GA.

Finally, the predicted uniaxial and biaxial tensile responses of the E-glass fiber-reinforced epoxy composites $[\pm 55]_{\text{T}}$ are compared with the stress–strain curves experimentally obtained by Soden [37]. The material properties adopted in the simulations are: $E_m = 2.6\,\text{GPa}$, $\upsilon_m = 0.4$; $E_f = 72.5\,\text{GPa}$, $\upsilon_f = 0.22$, $\phi_f = 60\%$. The GA calibration process is only carried out based on the uniaxial tensile loading case, and the model parameters are estimated to be: $\alpha = 2 \times 10^{-7}/\text{MPa}$, $\beta = 3 \times 10^{-7}/\text{MPa}$, $S = 9.79$, $M = 2$, $\varepsilon_{\text{th}} = 0.014$, $c_1 = 0.147$, $c_2 = 5.9$. It should be noted that the same values estimated for the model parameters are applied to the biaxial tensile loading cases.

Figure 12 shows comparisons between the present prediction and experimental data [37] for the uniaxial and biaxial tensile responses of $\pm 55°$ laminate composites. In spite of

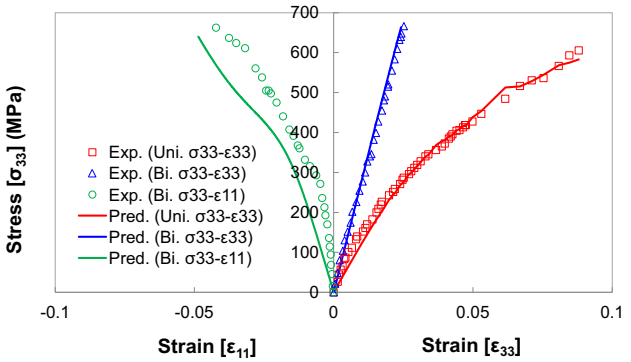

Fig. 12 Comparisons between the predicted values and experimental data for uniaxial and biaxial tensile responses of E-glass fiber-reinforced epoxy composites

some gaps between the prediction and the experimental result in the case of σ_{33}–ε_{11} under biaxial tensile loading, the predictions based on the proposed method match the experimental results well.

5 Conclusions

This paper presents a modeling strategy that relies on micromechanics and evolutionary computation to predict the damage behaviors of fiber-reinforced composites. The proposed framework, consisting of two methods, enables precise and efficient prediction of fibrous composites, not only with respect to external mechanical properties but internal failure mechanisms as well, including interfacial and micro-crack damage. Unlike previous analytical studies that have manually fitted the model parameters with experimental data, the present study introduces an advanced approach for the efficient and precise prediction of fibrous composites. Although the different modeling techniques considered here are based on different study backgrounds, they are coupled in the present study by the constitutive damage equation with several model parameters and the GA, while considering human-induced error components for fibrous composites.

It is shown that the model parameters of the proposed formulation influence the present predictions. The upper and lower bounds of each parameter are determined by referring to past research, and a numerical simulation which is independently performed in this study. The developed model is applied to various cases to predict the corresponding mechanical properties and stress–strain responses. Then, those predictions are compared with available experimental data in the literature to verify the proposed formulation, and were found to be well correlates with the test results. Interestingly, it is observed that the predicted damage patterns and progressions produced by the proposed approach with the GA depend strongly on the loading conditions, illustrating realistic damage responses.

This study would focus on multi-scale/physics modeling to obtain a clearer understanding of the changes in fibrous composites under various exterior conditions. In spite of the various validations conducted in this paper to ensure the predictive capabilities of the proposed method, future study should address the viscoelastic-related strain rate effects and more extreme cases should be considered to obtain better correlation between test conditions and composite compositions. These issues are beyond the scope of the present work; however, they should be considered in future work.

Appendix 1: The components of Eshelby's tensor $\mathbf{S}_2$ and $\mathbf{S}_3$ in Eq. (2)

The components of the fourth-rank Eshelby's tensors for the debonded cylindrical fiber (phase 2) are given as [38]

$$\mathbf{S}_2 = \frac{1}{4\left(1-v_0\right)}\left[S^{(3)}_{IK}\delta_{ij}\delta_{kl} + S^{(4)}_{IJ}\left(\delta_{ik}\delta_{jl}+\delta_{il}\delta_{jk}\right)\right] \quad (27)$$

in which

$$\begin{aligned}
&S^{(3)}_{11} = \frac{1}{2}\left(4v_0-2\right), \quad S^{(3)}_{22} = S^{(3)}_{12} = S^{(3)}_{21} = S^{(3)}_{11},\\
&S^{(3)}_{13} = 2v_0, \quad S^{(3)}_{23} = S^{(3)}_{13}, \quad S^{(3)}_{31} = S^{(3)}_{32} = S^{(3)}_{33} = 0\\
&S^{(4)}_{11} = \frac{1}{2}\left(3-4v_0\right), \quad S^{(4)}_{22} = S^{(4)}_{12} = S^{(4)}_{21} = S^{(4)}_{11},\\
&S^{(4)}_{13} = 1-v_0, \quad S^{(4)}_{23} = S^{(4)}_{31} = S^{(4)}_{32} = S^{(4)}_{13},\\
&S^{(4)}_{33} = 0
\end{aligned} \quad (28)$$

In addition, the Eshelby's tensor $\mathbf{S}_3$ for the spherical micro-crack void (phase 3) can be expressed as [38]

$$\mathbf{S}_3 = \frac{1}{15\left(1-v_0\right)}\left[S^{(5)}\delta_{ij}\delta_{kl} + S^{(6)}\left(\delta_{ik}\delta_{jl}+\delta_{il}\delta_{jk}\right)\right] \quad (29)$$

with

$$S^{(5)} = 5v_0 - 1, \; S^{(6)} = 4 - 5v_0 \quad (30)$$

where v_0 denotes the Poisson's ratio of the matrix.

Appendix 2: Parameters $F_{IK}{}^{(1)}$ and $F_{IJ}{}^{(2)}$ in Eq. (8)

The parameters of the fourth-rank tensor **F** are expressed as

$$F_{IK}^{(1)} = \phi_1 \Lambda_{IK}^{(1)} + \phi_2 \Lambda_{IK}^{(3)} + \phi_3 \Lambda^{(5)},$$
$$F_{IJ}^{(2)} = \frac{1}{2} + \phi_1 \Lambda_{IJ}^{(2)} + \phi_2 \Lambda_{IJ}^{(4)} + \phi_3 \Lambda^{(6)} \tag{31}$$

in which

$$\Lambda_{IK}^{(2m-1)} = \frac{B_{IK}^{(2m-1)}}{1 - 2\phi_m P_{KK}^{(2m)}} + \frac{B_{II}^{(2m)} Q_{IK}^{(m)}}{\phi_m P_{II}^{(2m)} - 1} + \sum_{R=1}^{3} \frac{B_{IR}^{(2m-1)} Q_{RK}^{(m)}}{2\phi_m P_{RR}^{(2m)} - 1}, \quad m = 1,\ 2$$
$$\Lambda_{IJ}^{(2m)} = \frac{B_{IJ}^{(2m)}}{2} \left(\frac{1}{1 - 2\phi_m P_{IJ}^{(2m)}} + \frac{1}{1 - 2\phi_m P_{JI}^{(2m)}} \right), \quad m = 1,\ 2$$
$$\Lambda^{(5)} = \frac{1}{3} \left\{ \frac{2B^{(6)}}{2\phi_3 P^{(6)} - 1} + \frac{3B^{(5)} + 2B^{(6)}}{1 - \phi_3 \left(3P^{(5)} + 2P^{(6)}\right)} \right\},$$
$$\Lambda^{(6)} = \frac{B^{(6)}}{1 - 2\phi_3 P^{(6)}} \tag{32}$$

with

$$\begin{Bmatrix} Q_{I1}^{(m)} \\ Q_{I2}^{(m)} \\ Q_{I3}^{(m)} \end{Bmatrix} = \begin{bmatrix} 1 - \phi_m \left(P_{11}^{(2m-1)} + 2P_{11}^{(2m)}\right) & -\phi_m P_{21}^{(2m-1)} & -\phi_m P_{31}^{(2m-1)} \\ -\phi_m P_{12}^{(2m-1)} & 1 - \phi_m \left(P_{22}^{(2m-1)} + 2P_{22}^{(2m)}\right) & -\phi_m P_{32}^{(2m-1)} \\ -\phi_m P_{13}^{(2m-1)} & -\phi_m P_{23}^{(2m-1)} & 1 - \phi_m \left(P_{33}^{(2m-1)} + 2P_{33}^{(2m)}\right) \end{bmatrix}^{-1} \cdot \begin{Bmatrix} -\phi_m P_{I1}^{(2m-1)} \\ -\phi_m P_{I2}^{(2m-1)} \\ -\phi_m P_{I3}^{(2m-1)} \end{Bmatrix}, \quad m = 1,\ 2 \tag{33}$$

In addition, the parameters $P_{IK}{}^{(1)}$ and $P_{IJ}{}^{(2)}$ in Eq. (33) are given by

$$P_{IK}{}^{(2m-1)} = 2S_{IK}^{(2m-1)} B_{KK}^{(2m)} + 2S_{II}^{(2m)} B_{IK}^{(2m-1)} + \sum_{R=1}^{3} S_{IR}^{(2m-1)} B_{RK}^{(2m-1)}, \quad m = 1,\ 2$$
$$P_{IJ}{}^{(2m)} = S_{IJ}^{(2m)} \left(B_{IJ}^{(2m)} + B_{JI}^{(2m)}\right), \quad m = 1,\ 2$$
$$P^{(5)} = 2S^{(5)} B^{(6)} + B^{(5)} \left(3S^{(5)} + 2S^{(6)}\right),$$
$$P^{(6)} = 2S^{(6)} B^{(6)} \tag{34}$$

with

$$B_{IK}^{(1)} = -\frac{Y_{IK}^{(1)}}{2\left(\bar{\mu} + S_{II}^{(2)}\right)}, \quad B_{IJ}^{(2)} = \frac{1}{4\left(\bar{\mu} + S_{IJ}^{(2)}\right)},$$
$$B_{IK}^{(3)} = -\frac{Y_{IK}^{(2)}}{2S_{II}^{(4)} - 1}, \quad B_{IJ}^{(4)} = \frac{1}{2\left(S_{IJ}^{(4)} - 1\right)},$$
$$B^{(5)} = \frac{-S^{(5)}}{\left(2S^{(6)} - 1\right)\left(3S^{(5)} + 2S^{(6)} - 1\right)},$$
$$B^{(6)} = \frac{1}{2\left(S^{(6)} - 1\right)} \tag{35}$$

in which

$$\begin{Bmatrix} Y_{I1}^{(1)} \\ Y_{I2}^{(1)} \\ Y_{I3}^{(1)} \end{Bmatrix} = \begin{bmatrix} \bar{\lambda} + 2\bar{\mu} + S_{11}^{(1)} + 2S_{11}^{(2)} & \bar{\lambda} + S_{21}^{(1)} & \bar{\lambda} + S_{31}^{(1)} \\ \bar{\lambda} + S_{12}^{(1)} & \bar{\lambda} + 2\bar{\mu} + S_{22}^{(1)} + 2S_{22}^{(2)} & \bar{\lambda} + S_{32}^{(1)} \\ \bar{\lambda} + S_{13}^{(1)} & \bar{\lambda} + S_{23}^{(1)} & \bar{\lambda} + 2\bar{\mu} + S_{33}^{(1)} + 2S_{33}^{(2)} \end{bmatrix}^{-1} \times \begin{Bmatrix} \bar{\lambda} + S_{I1}^{(1)} \\ \bar{\lambda} + S_{I2}^{(1)} \\ \bar{\lambda} + S_{I3}^{(1)} \end{Bmatrix} \tag{36}$$

and

$$\begin{Bmatrix} Y_{I1}^{(2)} \\ Y_{I2}^{(2)} \\ Y_{I3}^{(2)} \end{Bmatrix} = \begin{bmatrix} -1 + S_{11}^{(3)} + 2S_{11}^{(4)} & S_{21}^{(3)} & S_{31}^{(3)} \\ S_{12}^{(3)} & -1 + S_{22}^{(3)} + 2S_{22}^{(4)} & S_{32}^{(3)} \\ S_{13}^{(3)} & S_{23}^{(3)} & -1 + S_{33}^{(3)} + 2S_{33}^{(4)} \end{bmatrix}^{-1} \times \begin{Bmatrix} S_{I1}^{(3)} \\ S_{I2}^{(3)} \\ S_{I3}^{(3)} \end{Bmatrix} \tag{37}$$

with

$$\bar{\lambda} = \frac{\lambda_0\mu_1 - \lambda_1\mu_0}{(\mu_1 - \mu_0)\{3(\lambda_1 - \lambda_0) + 2(\mu_1 - \mu_0)\}},$$
$$\bar{\mu} = \frac{\mu_0}{2(\mu_1 - \mu_0)} \tag{38}$$

where the constants λ_q and μ_q $(q = 1, 2)$ signify the Láme constant and shear modulus of the matrix and fiber, respectively.

Appendix 3: Parameters of the effective stiffness in Eq. (14)

The components of the effective stiffness of the fibrous composites considering the fiber orientation (θ) read [22]
1st row:

$$\begin{aligned}
\bar{C}_{11} &= c^4\left(C_{11}^{(1)} + 2C_{11}^{(2)}\right) + c^2s^2\left(C_{13}^{(1)} + C_{31}^{(1)} + 4C_{13}^{(2)}\right) \\
&\quad + s^4\left(C_{33}^{(1)} + 2C_{33}^{(2)}\right), \quad \bar{C}_{12} = c^2C_{12}^{(1)} + s^2C_{32}^{(1)}, \\
\bar{C}_{13} &= c^4C_{13}^{(1)} + c^2s^2\left(C_{11}^{(1)} + C_{33}^{(1)} + 2C_{11}^{(2)}\right. \\
&\quad \left. + 2C_{33}^{(2)} - 4C_{13}^{(2)}\right) + s^4C_{31}^{(1)}, \\
\bar{C}_{15} &= cs\left\{c^2\left(-C_{11}^{(1)} + C_{13}^{(1)} - 2C_{11}^{(2)} + 2C_{13}^{(2)}\right)\right. \\
&\quad \left. + s^2\left(-C_{31}^{(1)} + C_{33}^{(1)} + 2C_{33}^{(2)} - 2C_{13}^{(2)}\right)\right\}
\end{aligned} \tag{39}$$

2nd row:

$$\begin{aligned}
\bar{C}_{21} &= c^2C_{21}^{(1)} + s^2C_{23}^{(1)}, \quad \bar{C}_{22} = C_{22}^{(1)} + 2C_{22}^{(2)}, \\
\bar{C}_{23} &= c^2C_{23}^{(1)} + s^2C_{21}^{(1)}, \quad \bar{C}_{25} = cs\left(C_{23}^{(1)} - C_{21}^{(1)}\right)
\end{aligned} \tag{40}$$

3rd row:

$$\begin{aligned}
\bar{C}_{31} &= c^4C_{31}^{(1)} + c^2s^2\left(C_{11}^{(1)} + C_{33}^{(1)} + 2C_{11}^{(2)} + 2C_{33}^{(2)} - 4C_{13}^{(2)}\right) \\
&\quad + s^4C_{13}^{(1)}, \quad \bar{C}_{32} = c^2C_{32}^{(1)} + s^2C_{12}^{(1)}, \\
\bar{C}_{33} &= c^4\left(C_{33}^{(1)} + 2C_{33}^{(2)}\right) + c^2s^2\left(C_{13}^{(1)} + C_{31}^{(1)} + 4C_{13}^{(2)}\right) \\
&\quad + s^4\left(C_{11}^{(1)} + 2C_{11}^{(2)}\right), \\
\bar{C}_{35} &= cs\left\{c^2\left(-C_{31}^{(1)} + C_{33}^{(1)} + 2C_{33}^{(2)} - 2C_{13}^{(2)}\right)\right. \\
&\quad \left. + s^2\left(-C_{11}^{(1)} + C_{13}^{(1)} - 2C_{11}^{(2)} + 2C_{13}^{(2)}\right)\right\}
\end{aligned} \tag{41}$$

4th row:

$$\begin{aligned}
\bar{C}_{44} &= c^2C_{23}^{(2)} + s^2C_{12}^{(2)}, \quad \bar{C}_{44} = c^2C_{23}^{(2)} + s^2C_{12}^{(2)}, \\
\bar{C}_{46} &= cs\left(C_{23}^{(2)} - C_{12}^{(2)}\right)
\end{aligned} \tag{42}$$

5th row:

$$\begin{aligned}
\bar{C}_{51} &= cs\left\{c^2\left(-C_{11}^{(1)} + C_{31}^{(1)} - 2C_{11}^{(2)} + 2C_{13}^{(2)}\right)\right. \\
&\quad \left. + s^2\left(-C_{13}^{(1)} + C_{33}^{(1)} + 2C_{33}^{(2)} - 2C_{13}^{(2)}\right)\right\}, \\
\bar{C}_{52} &= cs\left(C_{32}^{(1)} - C_{12}^{(1)}\right), \\
\bar{C}_{53} &= cs\left\{c^2\left(-C_{13}^{(1)} + C_{33}^{(1)} + 2C_{33}^{(2)} - 2C_{13}^{(2)}\right)\right. \\
&\quad \left. + s^2\left(-C_{11}^{(1)} + C_{31}^{(1)} - 2C_{11}^{(2)} + 2C_{13}^{(2)}\right)\right\}, \\
\bar{C}_{55} &= \left(c^4 + s^4\right)C_{13}^{(2)} + c^2s^2\left(C_{11}^{(1)} - C_{13}^{(1)} - C_{31}^{(1)}\right. \\
&\quad \left. + C_{33}^{(1)} + 2C_{11}^{(2)} + 2C_{33}^{(2)} - 2C_{13}^{(2)}\right)
\end{aligned} \tag{43}$$

6th row:

$$\bar{C}_{64} = cs\left(C_{23}^{(2)} - C_{12}^{(2)}\right), \ \bar{C}_{66} = c^2C_{12}^{(2)} + s^2C_{23}^{(2)} \tag{44}$$

where c and s denote the $\cos\theta$ and $\sin\theta$, respectively.

References

1. Gibson RF (2010) A review of recent research on mechanics of multifunctional composite materials and structures. Compos Struct 92:2793–2810
2. Liew K, Lei Z, Zhang L (2015) Mechanical analysis of functionally graded carbon nanotube reinforced composites: a review. Compos Struct 120:90–97
3. Lu K (2010) The future of metals. Science 328:319–320
4. Feraboli P, Miller M (2009) Damage resistance and tolerance of carbon/epoxy composite coupons subjected to simulated lightning strike. Compos Part A Appl Sci Manuf 40:954–967
5. Yang B, Ha S, Pyo S, Lee H (2014) Mechanical characteristics and strengthening effectiveness of random-chopped FRP composites containing air voids. Compos Part B Eng 62:159–166
6. Ju J, Chen TM (1994) Micromechanics and effective moduli of elastic composites containing randomly dispersed ellipsoidal inhomogeneities. Acta Mech 103:103–121
7. Ju J, Zhang X (1998) Micromechanics and effective transverse elastic moduli of composites with randomly located aligned circular fibers. Int J Solids Struct 35:941–960
8. Qu J (1993) The effect of slightly weakened interfaces on the overall elastic properties of composite materials. Mech Mater 14:269–281
9. Pyo S, Lee H (2010) An elastoplastic damage model for metal matrix composites considering progressive imperfect interface under transverse loading. Int J Plast 26:25–41
10. Kim B, Lee H (2010) Elastic-damage modeling for particulate composites considering cumulative damage. Int J Damage Mech 20:131–158
11. Lee H (2001) A computational approach to the investigation of impact damage evolution in discontinuously reinforced fiber composites. Comput Mech 27:504–512
12. Lee H, Simunovic S (2000) Modeling of progressive damage in aligned and randomly oriented discontinuous fiber polymer matrix composites. Compos Part B Eng 31:77–86
13. Lee H, Pyo S (2009) 3D-damage model for fiber-reinforced brittle composites with microcracks and imperfect interfaces. J Eng Mech 135:1108–1118

14. Yang B, Shin H, Lee H, Kim H (2013) A combined molecular dynamics/micromechanics/finite element approach for multiscale constitutive modeling of nanocomposites with interface effects. Appl Phys Lett 103:241903
15. Karihaloo B, Fu D (1989) A damage-based constitutive law for plain concrete in tension. Eur J Mech A Solids 8:373–384
16. Pyo S, Lee H (2009) Micromechanics-based elastic-damage analysis of laminated composite structures. Int J Solids Struct 46:3138–3149
17. Yang B, Shin H, Kim H, Lee H (2014) Strain rate and adhesive energy dependent viscoplastic damage modeling for nanoparticulate composites: molecular dynamics and micromechanical simulations. Appl Phys Lett 104:101901
18. Huang Z (2001) Micromechanical prediction of ultimate strength of transversely isotropic fibrous composites. Int J Solids Struct 38:4147–4172
19. Ju J, Yanase K (2011) Micromechanical effective elastic moduli of continuous fiber-reinforced composites with near-field fiber interactions. Acta Mech 216:87–103
20. Barai P, Weng GJ (2011) A theory of plasticity for carbon nanotube reinforced composites. Int J Plast 27:539–559
21. Taya M, Mura T (1981) On stiffness and strength of an aligned short-fiber reinforced composite containing fiber-end cracks under uniaxial applied stress. J Appl Mech 48:361–367
22. Herakovich CT (1998) Mechanics of fibrous composites. Wiley, New York
23. Liang Z, Lee H, Suaris W (2006) Micromechanics-based constitutive modeling for unidirectional laminated composites. Int J Solids Struct 43:5674–5689
24. Weibull W (1951) A statistical function of wide distribution. J Appl Mech 18:293–297
25. Yang B, Kim B, Lee H (2012) Predictions of viscoelastic strain rate dependent behavior of fiber-reinforced polymeric composites. Compos Struct 94:1420–1429
26. Mishnaevsky L Jr (2012) Composite materials for wind energy applications: micromechanical modeling and future directions. Comput Mech 50:195–207
27. Fraser AS (1960) Simulation of genetic systems by automatic digital computers VI. Epistasis. Aust J Biol Sci 13:150–162
28. Eberhart RC, Shi Y (2011) Computational intelligence: concepts to implementations. Elsevier, Amsterdam
29. Tabassum M, Mathew K (2014) A genetic algorithm analysis towards optimization solutions. Int J Dig Inf Wirel Commun (IJDIWC) 4:124–142
30. Weeks C, Sun C (1998) Modeling non-linear rate-dependent behavior in fiber-reinforced composites. Compos Sci Technol 58:603–611
31. Xia Z, Chen Y, Ellyin F (2000) A meso/micro-mechanical model for damage progression in glass-fiber/epoxy cross-ply laminates by finite-element analysis. Compos Sci Technol 60:1171–1179
32. Liu Z, Moore JA, Aldousari SM, Hedia HS, Asiri SA, Liu WK (2015) A statistical descriptor based volume-integral micromechanics model of heterogeneous material with arbitrary inclusion shape. Comput Mech 55:963–981
33. Herakovich CT (2012) Mechanics of composites: a historical review. Mech Res Commun 41:1–20
34. Li DS, Wisnom MR (1994) Unidirectional tensile stress–strain response of BP–SiC fiber reinforced Ti–6Al–4V. J Compos Technol Res 16:225–233
35. Luo J, Daniel I (2000) A cylinder model for characterization of deformation and damage development in a unidirectional composite. Compos Sci Technol 60:2791–2802
36. Naboulsi S (2003) Modeling composites transversely loaded metal-matrix. J Compos Mater 37:55–72
37. Soden P, Hinton M, Kaddour A (2002) Biaxial test results for strength and deformation of a range of E-glass and carbon fibre reinforced composite laminates: failure exercise benchmark data. Compos Sci Technol 62:1489–1514
38. Mura T (2013) Micromechanics of defects in solids. Springer, Berlin